ADVANCES IN ATMOSPHERIC SCIENCES, VOL. 35, APRIL 2018, 479–492

• **Original Paper** •

Validation and Spatiotemporal Distribution of GEOS-5–Based Planetary Boundary Layer Height and Relative Humidity in China

Yidan SI[1,2], Shenshen LI[*1], Liangfu CHEN[1], Chao YU[1], Zifeng WANG[1], Yang WANG[1,2], and Hongmei WANG[1,2]

[1]*State Key Laboratory of Remote Sensing Sciences, Institute of Remote Sensing and Digital Earth, Chinese Academy of Sciences, Beijing* 100101*, China*

[2]*University of Chinese Academy of Sciences, Beijing* 100049*, China*

(Received 23 November 2016; revised 21 July 2017; accepted 3 August 2017)

ABSTRACT

Few studies have specifically focused on the validation and spatiotemporal distribution of planetary boundary layer height (PBLH) and relative humidity (RH) data in China. In this analysis, continuous PBLH and surface-level RH data simulated from GEOS-5 between 2004 and 2012, were validated against ground-based observations. Overall, the simulated RH was consistent with the statistical data from meteorological stations, with a correlation coefficient of 0.78 and a slope of 0.9. However, the simulated PBLH was underestimated compared to LIDAR data by a factor of approximately two, which was primarily because of poor simulation in late summer and early autumn. We further examined the spatiotemporal distribution characteristics of two factors in four regions—North China, South China, Northwest China, and the Tibetan Plateau. The results showed that the annual PBLH trends in all regions were fairly moderate but sensitive to solar radiation and precipitation, which explains why the PBLH values were ranked in order from largest to smallest as follows: Tibetan Plateau, Northwest China, North China, and South China. Strong seasonal variation of the PBLH exhibited high values in summer and low values in winter, which was also consistent with the turbulent vertical exchange. Not surprisingly, the highest RH in South China and the lowest RH in desert areas of Northwest China (less than 30%). Seasonally, South China exhibited little variation, whereas Northwest China exhibited its highest humidity in winter and lowest humidity in spring, the maximum values in the other regions were obtained from July to September.

Key words: GEOS-5, planetary boundary layer height, relative humidity, validation, spatiotemporal distribution

Citation: Si, Y. D., S. S. Li, L. F. Chen, C. Yu, Z. F. Wang, Y. Wang, and H. M. Wang, 2018: Validation and spatiotemporal distribution of GEOS-5–based planetary boundary layer height and relative humidity in China. *Adv. Atmos. Sci.*, **35**(4), 479–492, https://doi.org/10.1007/s00376-017-6275-3.

1. Introduction

With the acceleration of urbanization in China, frequent haze events caused by high concentrations of fine particulate matter ($PM_{2.5}$) have received worldwide attention (Li et al., 2013, 2016). Research on the mechanism of haze formation and its effects on the climate and public health require long-term air pollution data. A national monitoring network for $PM_{2.5}$ and its precursor pollutants (e.g., NO_2 and SO_2) was not established in China until 2013. Satellite remote sensing can fill spatiotemporal gaps in ground-based observations. To date, numerous studies have been conducted to estimate the surface levels of $PM_{2.5}$ using satellite-retrieved aerosol optical depth (AOD) data (Wang and Christopher, 2003; Gupta et al., 2006; Koelemeijer et al., 2006). However, building an accurate AOD–$PM_{2.5}$ model remains a considerable challenge because the correlation between these two parameters is nonlinear. Because AOD reflects the aerosol optical properties of the entire air column, whereas $PM_{2.5}$ is usually measured at the surface level and under dry conditions, the AOD–$PM_{2.5}$ relationship depends heavily on the vertical aerosol profile and aerosol hygroscopic growth (Gupta et al., 2006; Guo et al., 2009). Currently, almost all quantitative AOD–$PM_{2.5}$ models include planetary boundary layer height (PBLH) and relative humidity (RH) data to reduce model uncertainty (Doukas et al., 2010; Wang et al., 2010). Therefore, the precision of the predicted $PM_{2.5}$ is strongly influenced by the quality of the included PBLH and RH data.

It is imperative to study the trends in PBLH and RH because rapid variations may contribute to extreme haze events (Zhou et al., 2005; Stott, 2016; Sun et al., 2016). The PBLH is important to consider in research on pollutant transport, the microphysics of clouds (Seibert et al., 2000; Medeiros et al., 2005), and weather and climate prediction (Hu et al., 2010). RH is closely related to the surface water and energy

* Corresponding author: Shenshen LI
Email: lishenshen@126.com

balance (Jones et al., 2010). Many recent studies have investigated the properties of the PBLH and RH using ground-based measurements. For example, Luo et al. (2014) developed different LIDAR-based methods based on systematic variations in planetary boundary layer structures over different surfaces and analyzed the diurnal and seasonal cycles of the PBLH over the land and ocean. Zhang et al. (2014) examined the PBLH over Yichang, China, from August 2006 to January 2007 using eight-times-daily sampling data from intensive radiosonde observations, and they found that the PBLH in both the summer and winter months exhibited diurnal changes, and that the daily cycle was deeper in the summer. For RH, Moradi et al. (2016) provided both qualitative and quantitative methods to illustrate the diurnal and spatial variations in tropospheric RH in tropical regions using Sondeur Atmosphérique du Profil d'Humidité Intertropicale par Radiométrie measurements. Vergados et al. (2015) explored the spatial variability in tropical tropospheric RH throughout the vertical extent of the troposphere and compared the spatial discrepancies in RH among the COSMIC, ERA-Interim and MERRA datasets. By simultaneously using LIDAR-retrieved PBLH, RH, and other meteorological parameters, Liu et al. (2013) investigated the formation and evolution mechanism of regional haze in the megacity of Beijing during 20–27 September 2011. Previous studies have primarily been conducted in high polluted areas or over a short period, because ground-based measurements usually cannot reflect the spatial variability in aerosols and meteorological parameters. To date, only a few studies have specifically focused on the PBLH and RH on a national scale and identified the associated spatiotemporal patterns in detail. For example, using fine-resolution, ground-based sounding data from across China, a comprehensive investigation of the PBL in China from January 2011 to July 2015 was conducted by Guo et al. (2016). This investigation revealed the climatology of the PBLH and its associations with atmospheric variables. Additionally, Zhang et al. (2016) used the radiosonde network in China to investigate CALIOP-derived PBLH on a large scale, and Liu et al. (2015) used CALIOP-derived PBLH data to evaluate the ECMWF's PBLH retrievals. These studies shed light on the data quality of the initial CALIOP-derived PBLH results; thus, they enhance our understanding of variations in the PBLH and how the PBLH mediates the exchange of energy and pollutants between the surface and atmosphere.

In addition to ground-based observations, numerical simulations have been widely used to derive the vertical aerosol structure and related meteorological parameters and support research on environmental and climate change. For example, the chemistry–aerosol–cloud–radiation–climate feedbacks were analyzed over the continental United States by determining the changes in the PBLH, temperature, and wind speed as simulated by the Weather Research Forecasting model (Zhang et al., 2010). The Pacific–North America teleconnection phase was found to influence sulfate concentrations, mainly through changes in the PBLH, precipitation, and temperature, based on results from the GEOS chemical transport model (Feng et al., 2016). Model-simulated PBLH and RH values can also fill gaps in surface observation–based estimates of $PM_{2.5}$ concentrations. For example, by incorporating the PBLH and RH simulated by the Regional Atmospheric Modeling System, the $PM_{2.5}$ concentrations over the North China Plain were estimated from MODIS AOD data (Tao et al., 2013).

GEOS-5 is a system of models integrated using the Earth System Modeling Framework. It was developed in NASA's Global Modeling Assimilation Office to support their earth science research in data analysis, observing system modeling and design, climate and weather prediction, and basic research (http://geos5.org/wiki/index.php?title=GEOS-5_Earth_System_Modeling_and_Data_Assimilation). GEOS-5 has been widely deployed all over the world to support the associated chemistry and transport modules (e.g., GEOS-Chem), but its applicability in China has rarely been examined. In addition, the simulated PBLH (or vertical aerosol distribution) and RH from GEOS data, combined with satellite-retrieved AOD data, have been widely used to estimate near-surface $PM_{2.5}$ concentrations. For example, Liu et al. (2004) first generated an annual mean $PM_{2.5}$ map for the United States in 2001, by scaling the model and satellite AOD. Ma et al. (2014) developed a national-scale geographically weighted regression model to estimate the daily $PM_{2.5}$ concentrations in China by coupling MODIS AOD and GEOS-5 meteorological data (including the PBLH, RH, wind speed, temperature, and other data). Therefore, the aim of the present study was to validate and analyze the variation tendencies and distribution of model-simulated PBLH and ground-level RH in China. Section 2 describes the study region and the various data used in the analysis. Section 3 presents the validation of the simulated results using ground-based data. Section 4 presents the analysis of the annual and seasonal distributions of the PBLH and RH in China. Finally, conclusions are provided in section 5.

2. Data and methods

2.1. *Study domain*

China lies between the latitudes of 18° and 54°N and the longitudes of 73° and 135°E. Its climate differs from region to region because of the country's highly complex topography. According to the different terrain and climatic conditions, the entire study domain can be divided into four regions: North China, South China, Northwest China and the Tibetan Plateau (TP). Barren land and desert are the main types of terrain in the Northwest China region (36°03′–48°10′N, 73°40′–120°58′E), and the Taklimakan Desert lies in this region. The TP (26°50′–39°15′N, 73°40′–104°57′E) is the largest plateau in China and the highest plateau in the world, and is dominated by masses of rock and a mountain plateau climate. The developed (and thus more polluted) regions in China include the North China (31°52′–53°33′N, 104°57′–135°2′E) and South China (3°30′–35°07′N, 97°51′–124°34′E) regions, which are divided by the line of the Qinling Mountains–Huaihe River.

Most of the North China region is covered by cultivated crops and forest. Northwest China is characterized by a temperate continental climate with warm and rainy summers but cold and dry winters. In South China, the land is relatively complex and includes large areas of wetland and grassland, as well as areas of dry land and forest. The region is characterized by a tropical to subtropical monsoon climate, with high temperatures and rain in summer and mild temperatures and less rainfall in winter.

2.2. *Data processing*

A nationwide ground-based LIDAR monitoring network has not been established in China due to the high expense of the equipment and the complexity of the operations involved. As a result, it is difficult to obtain large-scale PBLH data using ground LIDAR, particularly in the TP and Northwest China regions. In the present study, we only collected data from two LIDAR stations to evaluate the model simulations. As shown in Fig. 1, the stations were in Wuhan (29.97°N, 113.89°E; South China region) and Beijing (40°N, 116.38°E; North China region). Notably, dual-polarization LIDAR with a detection range of 3 km and a resolution of 3 m for vertical measurements is used at these two stations. In addition, 532 nm and 355 nm laser beams are simultaneously emitted from an Nd:YAG laser every 15 min, approximately, and the interactions of these beams with molecules and aerosols are used to investigate Rayleigh scattering and Mie scattering, respectively. The backscatter echo signals (BES) of atmospheric masses are gathered by the detector. The BES at 532 nm is divided into parallel channel and vertical channel signals, which can be used to calculate the depolarization ratio. The average value over a 3-h period [we defined fixed time intervals of 0800, 1100, 1400, 1700 and 2000 LST (Local Standard Time, LST=UTC+8)] was calculated to correspond to the model simulations and reduce the noise associated with the continuous LIDAR observations. In total, 72 records were collected during 16–31 December 2012 at Wuhan, and 154 records were collected during 5 August to 1 September 2008 at Beijing.

As the layer of the troposphere that is closest to the surface of the Earth, the PBL is directly influenced by the Earth's surface and responds to surface forcing at a timescale of approximately one hour or less (Guo et al., 2016). The thermal inversion layer that lies between the top of the boundary layer and the free atmosphere constrains convection activity, such as the movement of water vapor and pollutants, which causes aerosol particles to become concentrated in the PBL (Hägeli et al., 2000; Veerabuthiran et al., 2011; Liu et al.,

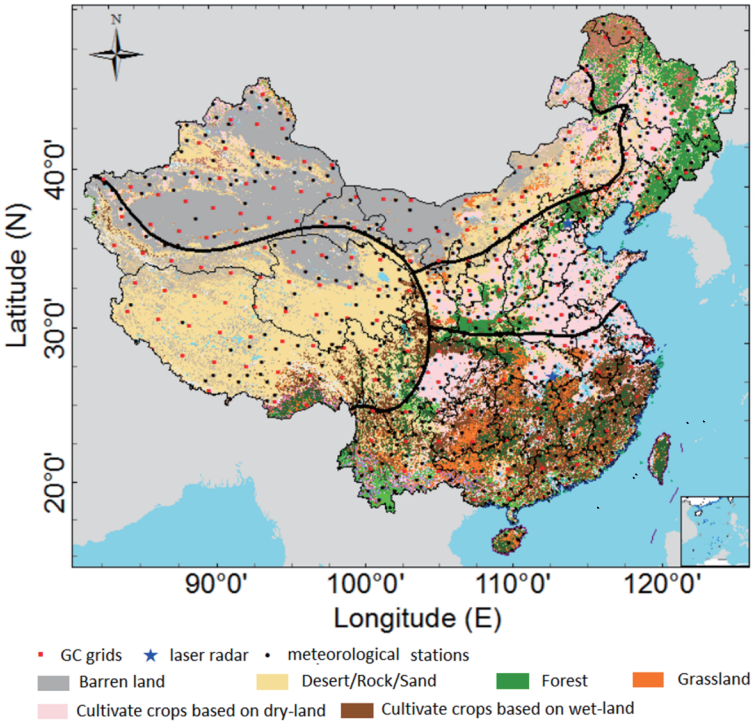

Fig. 1. Spatial distribution of the ground-based observation sites (blue stars and black points) and the $2^\circ \times 2.5^\circ$ grids (red squares) of GEOS-5. The black lines divide China into the North China, South China, Northwest China, and TP regions. The blue stars indicate the two ground-based LIDAR systems used to detect the PBLH, which are located in the cities of Beijing (North China region) and Wuhan (South China region). The black points indicate the 824 meteorological stations with RH data from 2004 to 2012. The land classification data were provided by the Multi-resolution Land Characteristics Consortium.

2015). Over land, the PBL follows a course that typically responds to the sensible heat flux at the surface (Hennemuth and Lammert, 2006). Specifically, during periods of strong daytime convection, aerosols are uniformly distributed in the vertical direction, due to the full development of the mixing layer. As a result, the extinction coefficient decreases sharply at the top of the boundary layer, and the position reflected by an obvious break in the LIDAR signal is defined as the PBLH (Chen et al., 2009; Chi et al., 2009; Veerabuthiran et al., 2011). Around sunset, a stable boundary layer evolves in which mechanically generated turbulence is damped by stability effects, which corresponds to the height of the top of the previous day's residual layer. Using the equation proposed by Fernald et al. (1972), the vertical distribution of the aerosol extinction coefficient was obtained from backscattered signals (Hennemuth and Lammert, 2006). The gradient method, also called the first derivation method, is commonly used to derive the PBLH from vertical profiles of the aerosol extinction coefficient, determining that the method is sensitive to the advection of an aerosol layer in the residual layer, above the mixed layer (Hayden et al., 1997). The uncertainties of the gradient method are related to the presence of signal noise, atmospheric variability (Li et al., 2017), cloud droplets, humidity (Menut et al., 1999) chemical pollutants (Hayden et al., 1997), and other factors. Figure 2 illustrates a time series of attenuated backscatter signals detected by dual-polarization LIDAR during 5–15 August 2008 over Beijing. Generally, the PBLH is below 1 km at the beginning and end of each day (sunrise and sunset). However, Fig. 2 shows that residual nighttime aerosol contributes to several peaks in extinction coefficients and PBLHs greater than 1 km, such as during nighttime on 8 August and in the morning hours of 9 August. The extinction values correspond to a height above 1 km on 14 August 2008, which was a rainy day with a cloud layer concentrated at ~ 4.5 km.

The PBL scheme employed in GEOS-5 uses the Lock et al. (2000) scheme for unstable layers and the Louis et al. (1982) scheme in stable shear-driven regimes, based on the method of turbulence parameterization and the Richardson number, respectively, as described in detail by McGrath-Spangler and Molod (2014). The PBLH is derived from vertical profiles of the diffusion coefficient, which depend on atmospheric properties at different altitudes. The final diffusion coefficient represents the vertical mixing by all turbulent processes, including surface and cloud-top buoyancy production and shear production. The PBLH simulated from GEOS-5 is defined as the height of the lowest layer in which the diffusivity falls below a threshold (https://gmao.gsfc.nasa.gov/products/documents/GEOS-5_Filespec_Glossary.pdf). The RH parameterized from GEOS-5 is approximated by q/q_s, where q is the specific humidity and q_s is its saturated value, with consistency of the RH dataset collected from meteorological monitoring stations.

In the present study, the simulated PBLH and near-surface RH data were directly obtained from GEOS-5 between 2004 and 2012 at a 3-h temporal resolution, i.e., 0000, 0300, 0600, 0900, 1200, 1500, 1800 and 2100 UTC (corresponding to 0800, 1100, 1400, 1700, 2000, 2300, 0200 and 0500 LST, respectively), and a 2° (latitude) ×2.5° (longitude) horizontal resolution. As shown in Fig. 1, there were 197 GEOS-5 grid cells in China. The China Meteorological Data Sharing Service System (http://cdc.nmic.cn/home.do) provides surface meteorological datasets of ground-level RH, temperature, precipitation and other parameters collected from 824 meteorological stations. The original RH data used in this study were measured at 0800, 1400, 2000 and 0200 BJT in the same geographic region as GEOS-5. Based on the sampling times of the original RH data, GEOS-5 RH data collected at the same times were extracted. The daily and monthly means were then calculated using hourly values to lessen the effects caused by outliers. Spatially, the observation data from all stations inside each GEOS-5 grid cell ($2^\circ \times 2.5^\circ$) were further averaged to match with the model simulations.

Notably, the PBLH estimation algorithm based on LIDAR differs from model simulation results. As previously discussed, LIDAR detects the height of the top of the previous day's residual layer and is perturbed by cloud droplets, which are three to four orders of magnitude larger than the signal backscattered by the aerosols. In GEOS-5, the PBLH derived from vertical profiles of the diffusion coefficient is treated as the height of the lowest layer in which the diffusivity falls below a threshold; for example, this is defined as 2 $m^2\ s^{-1}$ in the operational file. According to the PBLH defini-

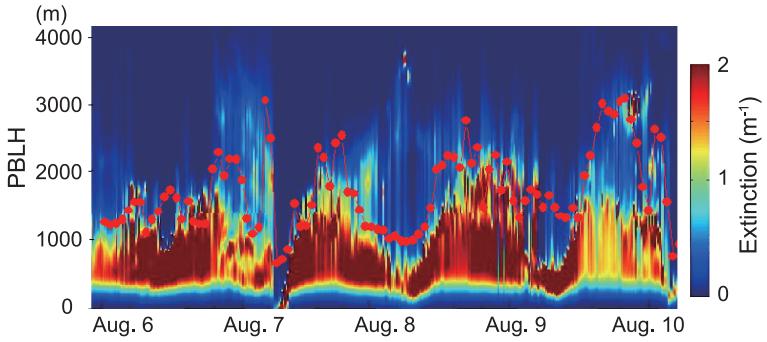

Fig. 2. Time series of attenuated backscatter signal (color bar) and boundary layer depth derived from dual-polarization LIDAR using the samples from 6–10 August 2008 at Beijing.

tion in GEOS-5 and the results extracted from the model used in this study, we can use the modeled PBLH to estimate the vertical extent of surface-connected turbulence, including in layers above the surface level. This approach differs from the LIDAR method, which relies on the vertical distribution of the aerosol extinction coefficient. This is a major contributor to the large difference between LIDAR-detected and model-simulated values in this analysis.

3. Results and discussion

3.1. *Validation of the PBLH*

Table 1 provides the mean, maximum and minimum values for both the model and in-situ data at the five collection times. The hourly comparisons show that the ground-based values of maximum PBLH exhibited a wider range (Wuhan: 1.844 km; Beijing: 2.850 km) at 0800 LST compared with the range of the model estimates (Wuhan: 0.333 km; Beijing: 0.417 km). The model simulations exhibited good agreement with the average PBLH values at three times (1100, 1400 and 1700 LST) of the daytime field measurements. As shown in Table 1, the discrepancy between the model and in-situ observations in Wuhan was less than 100 m. By contrast, the times when the model underestimated the PBLH relative to that based on ground observations were mainly in the morning and evening. For example, the mean values of the ground-based PBLH in Beijing at 0800 LST (1.711 km) and 2000 LST (2.137 km) were approximately six to seven times higher than the model-simulated values (0800 LST: 0.210 km; 2000 LST: 0.373 m). Clearly, the LIDAR-detected PBLH is the top of the residual layer but not the top of mixing layer.

Although no specific method for determining the detection error of the PBLH has been developed, findings from the comparison of multiple measurements (Emeis et al., 2004) or ground-based LIDAR with different data sources (Liu et al., 2015) have provided insight into the accuracy of ground-detected PBLH estimates during the daytime. These findings have demonstrated that ground-based, LIDAR-detected PBLH values are comparatively robust, although some bias can be attributed to instrument accuracy, the signal-to-noise ratio, and other factors. Figure 3 presents a comparison of the variations in the PBLH, as measured three times daily (1100, 1400 and 1700 LST) at a high confidence level, between the GEOS-5 and ground-based LIDAR values. The mean values of the simulated PBLH in both Wuhan (0.687 km) and Beijing (1.408 km) were low-biased compared with the ground data (Wuhan: 0.761 km; Beijing: 2.232 km). Specifically, Beijing exhibited larger bias (0.824) and RMSE (0.385) values than Wuhan (bias: −0.074; RMSE: 0.227). The sampling period in Beijing was in late summer and early autumn, when turbulent vertical exchange in the atmospheric boundary layer is extremely intense. However, the GEOS-5 model is not sensitive to abrupt variations in weather conditions or pollution from near-surface emissions or long-term transport (Li et al., 2015). The coarse resolution of GEOS-5 may contribute to large uncertainties. In addition, the PBLH values in Beijing used in this study were larger than those in Wuhan. To eliminate the impact of the PBLH discrepancies and achieve a reasonable comparison in different regions, we used the Q-value, defined as the ratio of the difference between the GEOS-5 and LIDAR-detected PBLH divided by the LIDAR-detected value ($|\mathrm{PBLH_{Model}} - \mathrm{PBLH_{lidar}}|/\mathrm{PBLH_{lidar}}$). Based on this equation, 25% and 77% of the GEOS-5 simulated RH in Beijing were located in the range of "$Q_{0.25} : (1 \pm 0.25) \times \mathrm{PBLH_{lidar}}$" and "$Q_{0.5} : (1 \pm 0.5) \times \mathrm{PBLH_{lidar}}$", respectively, which were more comparable with the Q-values in Wuhan ($Q_{0.25}$ = 36%; $Q_{0.5}$ = 74%). Overall, despite the significant underestimation by the model, GEOS-5 can be used to perform trend analyses, based on the similar variations and trends observed in this study.

3.2. *Validation of RH*

Figure 4 illustrates the validation of GEOE-5 RH using surface meteorological data. The number of daily mean RH records from 2004 to 2012 in China is 528 150. A linear regression of GEOS-5 data against data from meteorological stations yielded a correlation coefficient (r) of 0.78, a slope

Table 1. Mean, maximum and minimum values based on GEOS-5 and field measurements of the PBLH at five sampling times in Wuhan and Beijing. N is the matched sample size of PBLH between LIDAR and the model simulations in each station. AVG indicates the average of all the matched samples at each time. MAX and MIN are the maximum and minimum values, respectively, for all the matched samples at each time. The units of the PBLH are meters.

		Wuhan				Beijing			
Time (LST)		N	AVG	MAX	MIN	N	AVG	MAX	MIN
0800	LIDAR	15	0.503	1.844	0.245	27	1.712	2.850	0.872
	Model		0.167	0.333	0.066		0.210	0.417	0.080
1100	LIDAR	14	0.585	1.165	0.297	27	1.911	2.854	1.154
	Model		0.399	0.528	0.250		1.047	1.495	0.579
1400	LIDAR	14	0.819	1.423	0.488	28	2.347	3.031	1.234
	Model		0.872	1.171	0.619		1.588	2.404	0.855
1700	LIDAR	14	0.865	2.014	0.435	27	2.353	2.941	1.417
	Model		0.776	0.991	0.570		1.551	2.311	0.801
2000	LIDAR	15	0.600	1.516	0.283	26	2.137	2.868	1.034
	Model		0.190	0.676	0.078		0.373	0.781	0.142

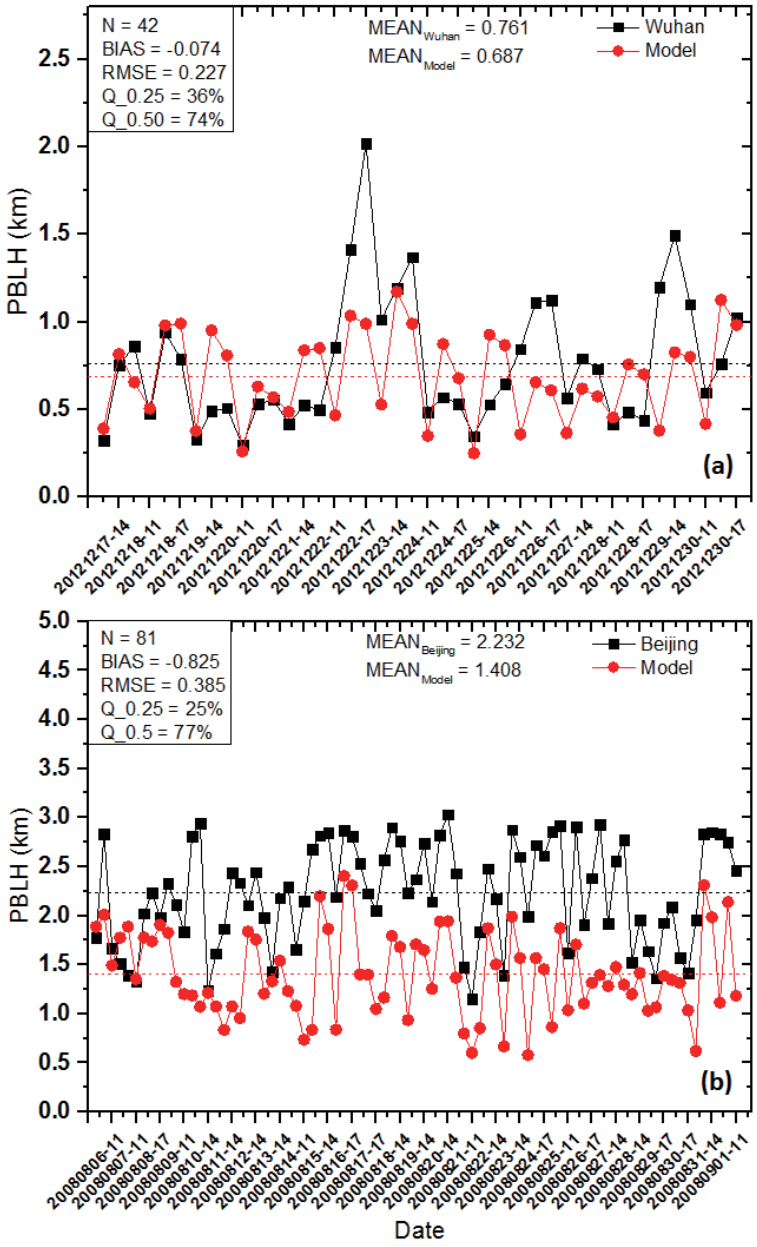

Fig. 3. Comparison of hourly PBLH values between ground-based observations (black points) and GEOS-5 (red points) values during the given period in the cities of (a) Wuhan and (b) Beijing.

of 0.9, an intercept of 3.26, and an RMSE of 14.31%, which indicated that the simulated RH strongly agrees with LIDAR measurements. The density of the points in Fig. 4a shows that most of the RH values were concentrated in the range of 70% to 85%. To make the comparison results clearer, the monthly mean values were calculated to reduce the daily uncertainties of samples. Thus, the number of points was reduced to 17 500, as shown in Fig. 4b. As expected, the monthly average results appeared to significantly reduce the noise in the daily RH. The correlation coefficient and slope increased to 0.83 and 0.96, respectively, compared to the daily average, whereas the intercept and RMSE decreased to −0.60 and 10.91, respectively. However, the model results were often overestimated for humid conditions (RH > 75%) and underestimated for dry conditions (RH < 75%). The locations of meteorological stations and the coarse spatial resolution of GEOS-5 likely contributed to the discrepancies between the model and ground-based data. Therefore, although the GEOS-5 horizontal resolution in this study was 2° (latitude) ×2.5° (longitude), our validation analysis shows that the simulated RH data can be used to replace field measurements to some extent, e.g., in remote sensing studies of $PM_{2.5}$.

The summary statistics for the GEOS-5 simulated and meteorologically observed RH values in different seasons and

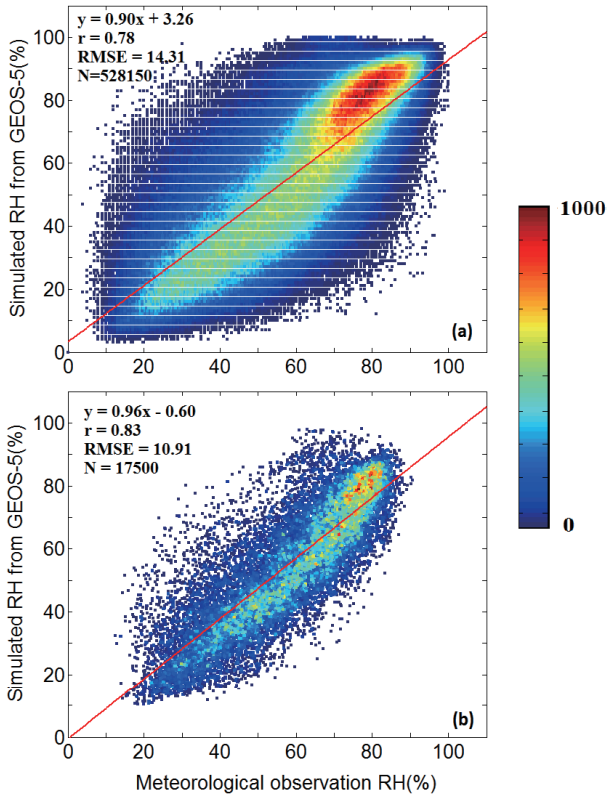

Fig. 4. Validation of GEOS-5-based simulations of (a) daily and (b) monthly mean RH values using meteorological observations. The linear regression is shown as the red line. The color bar represents the number of points with particular ordered pair values.

regions are presented in Table 2. Seasonally, the RH values simulated by GEOS-5 were generally lower than ground observations. The correlation coefficient was higher in spring (0.8) and summer (0.82) than in fall (0.76) and winter (0.69). Additionally, the slopes in summer (1.02) and fall (0.95) were greater than those in spring (0.87) and winter (0.75). Although the correlation was worst in winter, the mean GEOS-5 RH value (59.07%) was more comparable with the meteorological observations (60.61%) in winter than during other seasons. Geographically, the eastern sites (including the North and South China regions) generally exhibited higher RH values than the western sites (including the Northwest China and TP regions). Except for the overestimation in the TP (GEOS-5: 53%; ground: 49.79%), GEOS-5 notably underestimated the observed ground values in the other regions, particularly in Northwest China (GEOS-5: 49.94%; ground: 38.89%). Linear regression analysis showed that the slope between the GEOS-5 estimates and meteorological observations was highest in the North and South China regions, at 0.89, whereas the correlation coefficient was highest in Northwest China (0.75). The results for the TP were the worst among the four regions, with a corresponding slope of 0.72, coefficient of 0.65, intercept of 18.81, and RMSE of 15.45.

3.3. *Spatiotemporal distribution of the PBLH*

Based on the times of 1100, 1400 and 1700 LST, annual, seasonal and monthly means were calculated to assess the associated spatial distributions and seasonal characteristics. Figure 5 presents the annual variation in the GEOS-5 PBLH over the entire country and the four regions from 2004 to 2012. At the national scale, the nine-year variation was quite gradual, and the simulated PBLH values were approximately stable at 0.7 km. Overall, a gradual increasing trend was observed from 2004 to 2007, with small decreases in 2009 and 2010 and a decrease to the 2008 level in 2011.

Table 2. Comparison of the RH between meteorological observations and GEOS-5-based simulations in different seasons and geographical regions. *N* is the matched sample size of RH between LIDAR and the model simulations by seasons and regions. *r* is the correlation coefficient of comparisons of in situ measurements against GEOS-5 simulations by seasonally and geographically.

		N		Mean	Slope	Intercept	*r*	RMSE
Season								
	Spring	144 900	In situ	54.30	0.87	3.95	0.80	14.02
			GEOS-5	48.85				
	Summer	124 600	In situ	67.11	1.02	−5.06	0.82	13.49
			GEOS-5	59.32				
	Fall	127 400	In situ	63.44	0.95	−2.16	0.76	14.09
			GEOS-5	55.87				
	Winter	13 1250	In situ	60.61	0.75	14.45	0.69	14.65
			GEOS-5	59.07				
Region								
	North	13 2792	In situ	65.41	0.89	1.93	0.73	13.93
			GEOS-5	57.07				
	South	13 8828	In situ	77.70	0.89	7.78	0.72	10.11
			GEOS-5	73.83				
	Northwest	14 7882	In situ	49.94	0.80	0.23	0.75	12.77
			GEOS-5	38.89				
	Tibet	10 8648	In situ	49.79	0.72	18.81	0.65	15.45
			GEOS-5	53.00				

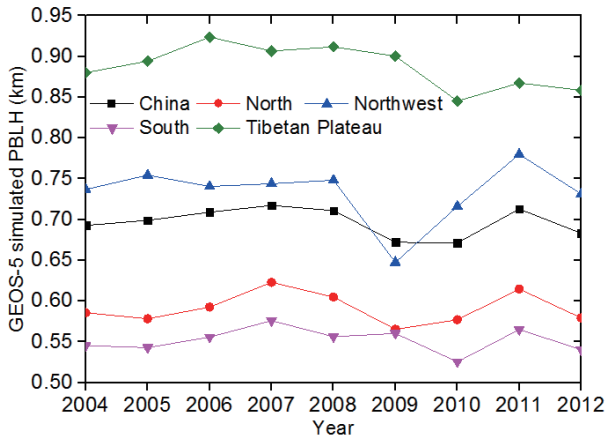

Fig. 5. Trend in the annual mean PBLH simulated from GEOS-Chem in China, North China, South China, Northwest China and TP China regions from 2004 through 2012 based on the times of 1100, 1400 and 1700 LST.

The final values were slightly lower than those in 2004 and higher than the minimum value, which was observed in 2012 (0.671 km). We found the low PBLH value at the national scale was due to the sudden decrease in the PBLH in Northwest China. Geographically, the PBLH in North China was similar to that nationally, and the values remained close to 0.6 km. The PBLH values (~ 0.55 km) in South China were the lowest, which was likely due to the influences of frequent rain and low solar radiation in this region. Additionally, the variations in this region were smallest among those in the four regions. According to the land cover data shown in Fig. 1, desert and barren land are the main land types in Northwest China. In addition, atmospheric circulation in these regions is very complex. These two factors resulted in a significant change in the PBL and a comparatively deep PBLH. For example, the PBLH values slowly increased from 2004 to 2008, sharply decreased to a minimum value in 2009 (~ 0.65 km), and then linearly increased to a peak value for the entire study period (~ 0.78 km) in the following two years. This trend may have been because of the abnormal climate conditions in this region in 2009. For example, Inner Mongolia experienced extremely low temperatures over a wide area and long period in winter 2009. The annual mean PBLH values were the highest in the TP region (> 0.85 km) because the high altitude and intense solar radiation in the region cause dramatic variations in the atmospheric structure.

Figure 6 shows the distribution of the seasonal mean PBLH across China from 2004 through 2012. Notably, the PBLH over China exhibited seasonal variation, with high values in summer (June, July and August) and low values in winter (December, January and February), when the development of the PBL is typically suppressed due to the low amount of solar radiation received at the surface. These seasonal features are consistent with the results of Zhang et al. (2016), who studied the CALIOP-derived PBLH climatology throughout China using satellite-based LIDAR. They found that CALIOP-derived PBLH can be used as a benchmark for comparison with model-simulated PBLH. During seasons with frequent haze events (e.g., winter), due to the suppression caused by aerosol radiative effects and aerosol–wind interaction, a shallow PBLH is apparent across most of China. This result agrees with previous findings (Quan et al., 2013; Miao et al., 2016); for example, Wang et al. (2010) and Gao et al. (2015) observed negative correlations between pollutants and the PBLH. In the present study, geographically, the PBLH was slightly higher in spring (March, April and May) and summer than in other seasons in the North China region because of strong mechanical forcing and synoptic patterns, such as the strong northwesterly thermal conditions that significantly modulate boundary layer processes (Miao et al., 2015). The lowest PBLH (0.12–0.5 km) values occurred in winter. This effect was particularly evident in the northeastern part of the North China regions. Notably, temperatures of approximately −20°C are not conducive to forming a strong thermal effect. In South China, the PBLH values were largely independent of season. The values of 0.5–0.65 km in spring and summer were higher than the values of 0.35–0.5 km in fall and winter. Differences in the thermal effect between the ocean and mainland may have contributed to higher PBLH values (> 0.65 km) in the coastal regions of North China and South China during the colder seasons and lower values (< 0.5 km) during the warmer seasons, whereas inland regions exhibited the opposite trend. Our results are consistent with those of Zhang et al. (2013), who observed high PBLH values over Hainan Island in fall and winter.

The seasonal variations were most obvious in the Northwest China region. The average PBLH values in summer were at least three times as high as those in winter (0.12–0.35 km), which is in good agreement with the results of Ma et al. (2011). The PBLH over the TP region was characterized by high values that varied geographically, with an average over the entire year greater than 0.8 km. The values in the eastern TP were lower than those in other areas, and the difference between these values reached 0.4 km. The spatial distribution of the PBLH revealed a tendency toward higher PBLHs in high-elevation regions, which was consistent with the dependence on elevation reported in studies in the United States (Seidel et al., 2012) and China (Zhang et al., 2016).

To obtain more detail regarding the different regional variations in each season, the average PBLH values in the same month from 2004 to 2012 were examined. As presented in Fig. 7, the monthly mean PBLH across China was positively correlated with the temperature changes in different months, with high peak concentrations from April to August, low values in winter, and an approximately symmetrical distribution across the entire year. Geographically, a similar trend appeared in the North China region, with a maximum value (0.91 km) in July and minimum (0.32 km) in January. In South China, the climate type determined the PBLH trend, which was the most moderate among those in all the study regions. The values were generally stable and between 0.45 km and 0.6 km. In the Northwest China region, the monthly average values fluctuated considerably because the cumulative effect of frequently continuous clear days was particularly

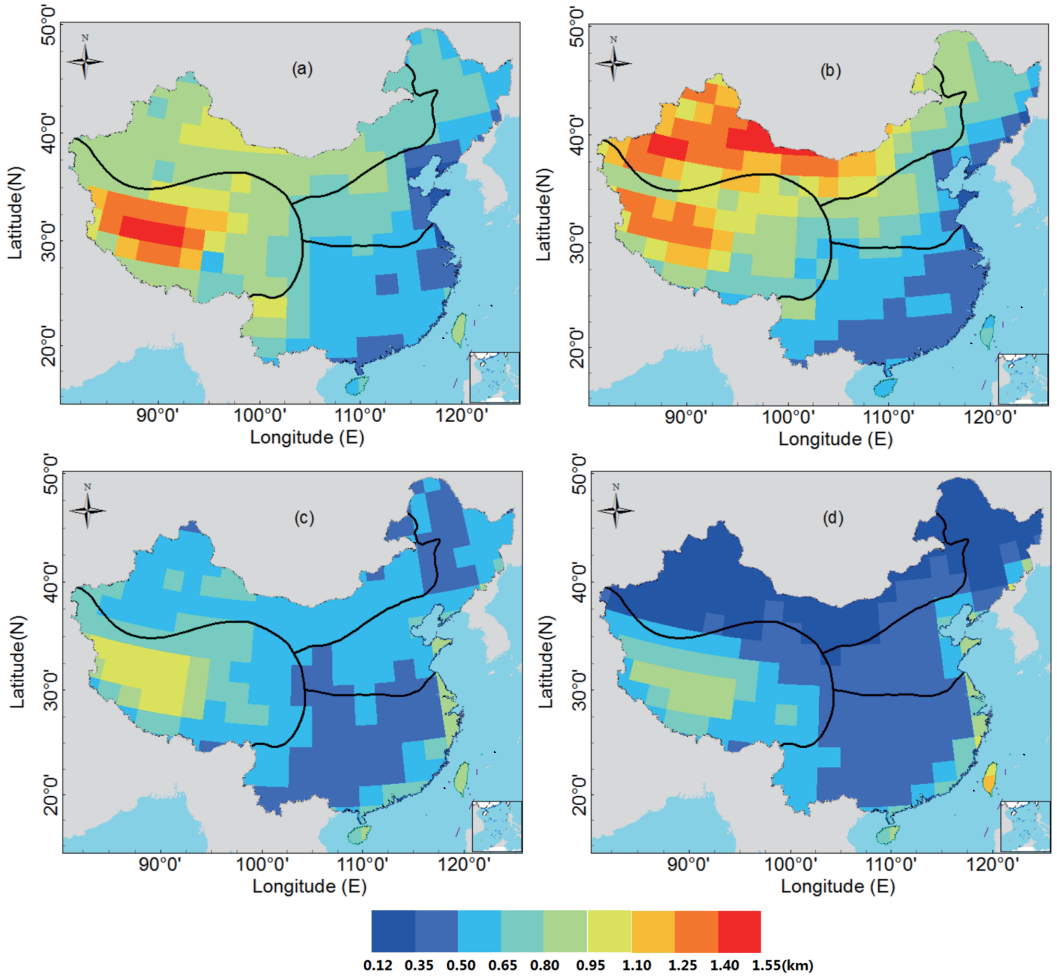

Fig. 6. Distribution of the seasonal average PBLH (km) in China from 2004–2012 in (a) spring (March, April, May), (b) summer (June, July, August), (c) fall (September, October, November), and (d) winter (December, January, February).

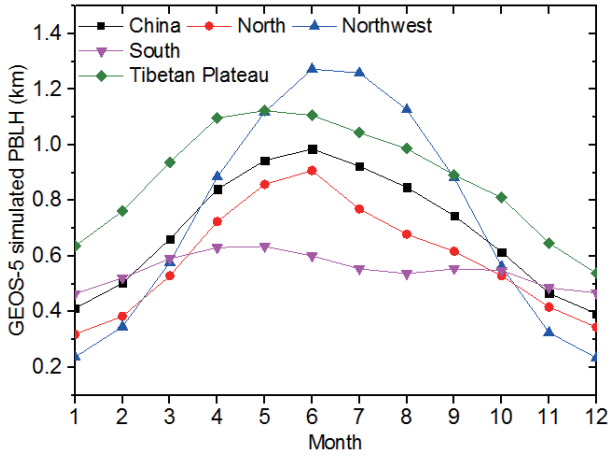

Fig. 7. Trend in the monthly average PBLH in different regions from 2004 through 2012.

significant from May to August, as were the influences of surface heating and atmospheric dynamics. For example, the maximum value in June (1.273 km) was six times higher than the minimum value in December (0.234 km). In the TP, the variations were similar to those in China, but the average PBLH was higher overall than those in other regions. High values (1.11 km) were observed from April to May, which was an earlier period than noted in the North and Northwest China regions.

3.4. *Spatiotemporal distribution of RH*

Figure 8 shows the variation in the annual mean RH from 2004 to 2012. At the national scale, the nine-year trend was within the narrow range of 51% to 57%. Geographically, all four regions exhibited similar trends but with different magnitudes and ranges. In North China, the RH values (52%–60%) were slightly higher than those across China, which indicated the climate type was comparatively moderate with respect to rainfall. The RH decreased obviously from 2004 through 2009. Our results are also consistent with the downward trend observed using ground-based data in a previous study (Song et al., 2012). The South China region is characterized by abundant rainfall and moist air throughout the year, in addition to frequent irrigation from rivers and lakes,

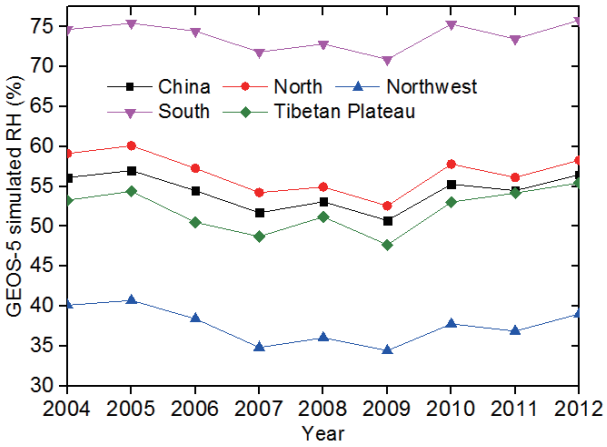

Fig. 8. As in Fig. 4 but for RH.

which contributed to the higher RH values than those in the other regions, and the minimum RH was greater than 70%. By contrast, Northwest China is far from the ocean, and the land cover of the region consists of desert and barren soil. The annual precipitation decreases from approximately 400 mm in the east to 200 mm in the west and, at times, to below 50 mm. Therefore, the lowest RH values appeared in this region, with a maximum of 41% in 2005. Although the TP lacks precipitation and has strong radiation and few forests, other factors, e.g., the many mountains covered with snow and glaciers, led to RH values in the range of 47% to 56%. The evaluation of long-term meteorological data provided by Zhang et al. (2011) indicated that the variation in RH from 2004 to 2012 strongly affected the trend in annual precipitation.

Figure 9 shows the seasonal distribution of RH from 2004 through 2012. The variation in North China was complicated. In Northeast China, the RH increased gradually throughout the year (spring, summer, fall and winter). On the North China Plain, the prevailing north-deflected airflow, which is a relatively weak, warm and humid flow, coupled with the unbalanced relationship between cold and warm air (Zhu et al., 2011), create conditions that are ideal for a lack of rain from March to May, with the wettest conditions in summer and driest conditions in spring. The South China region, which has a mild climate, exhibited no significant changes throughout the entire year, with high RH levels of 80%–100%. As expected, the Northwest China region received scarce precipitation, particularly in the Taklimakan Desert, due to its long distance from the ocean and the presence of a topographic barrier that prevents the transport of moist air; thus, this region had the lowest RH value of 19% (Fig. 9a). Except for winter, all seasons were dry in the Northwest China region. This finding is similar to that of Xu et al. (2015), who reported that precipitation in Urumqi increased sharply in winter. In the TP region, the RH values in the southeastern part were higher than those in other parts because it is cold and dry in the northwest and warm and wet in the southeast.

Figure 10 shows the monthly variation in RH in the different regions. Nationwide, the variation in the trend first declined and then increased twice over the entire year, with low values from March to May and October to November and high values between January and February and between July and August. Specifically, the values in April and May were less than 50%, whereas those in January, July and August were approximately 60%. The variation in North China was similar but with slightly more abrupt than those in China overall, with peak values of approximately 66% and trough values of 45%. Because the precipitation in North China is primarily concentrated in summer, the RH values in this region peaked (66%) in July and August. Additionally, high RH values were observed from December to February and may have been caused by the low evaporation and snow cover throughout northeastern China. The rainy season in South China starts each year in May and continues until September, when the summer monsoon makes landfall from the coastal areas of the region. Therefore, the RH values in the South China region were far higher than those in the other regions, with a maximum in August (81%) and minimum in December (70%). The RH in the Northwest China region was the lowest in the country and varied considerably throughout the year. High RH values were observed in November through to the following February. This result was likely observed because the snow stages are concentrated in winter, and the low temperatures are not conducive to evaporation (Dandou et al., 2009). By contrast, the RH gradually decreased, starting in spring, due to a rapid increase in the surface temperature and disappearing snow cover, which resulted in relatively dry conditions from March until October. As illustrated by the pink line in Fig. 10, the trend in the TP region was completely associated with the influence of the rainy season. Thus, the climate from May to September each year is naturally wet.

3.5. *Discussion*

The application of satellite remote sensing to $PM_{2.5}$ prediction has evolved greatly in China. Many recent studies have established the AOD–$PM_{2.5}$ relationship using advanced statistical models. These studies included meteorological parameters (e.g., PBLH, RH, temperature, and wind speed) as covariates to improve model performance. However, meteorological parameters have not been as widely investigated as satellite AOD. To the best of our knowledge, previous studies have not specifically focused on the effects of the PBLH and RH on $PM_{2.5}$ satellite prediction. For example, although a geographically weighted regression model and two-stage spatial statistical model can accurately predict $PM_{2.5}$ concentrations with little bias at the seasonal level, they yield relative prediction errors of greater than 30% at the daily scale (Ma et al., 2016). Based on our sensitivity analysis of prediction models, and personal communications with Zongwei MA and Yang LIU (2016), we found that predicted $PM_{2.5}$ concentrations are typically negatively correlated with PBLH and RH data. Thus, high PBLH or RH values from GEOS-5 yield low model estimates of $PM_{2.5}$ concentrations. In this study, the modeled PBLH was generally lower than the LIDAR-based PBLH; therefore, the final $PM_{2.5}$ was often overestimated. The impact of GEOS-5

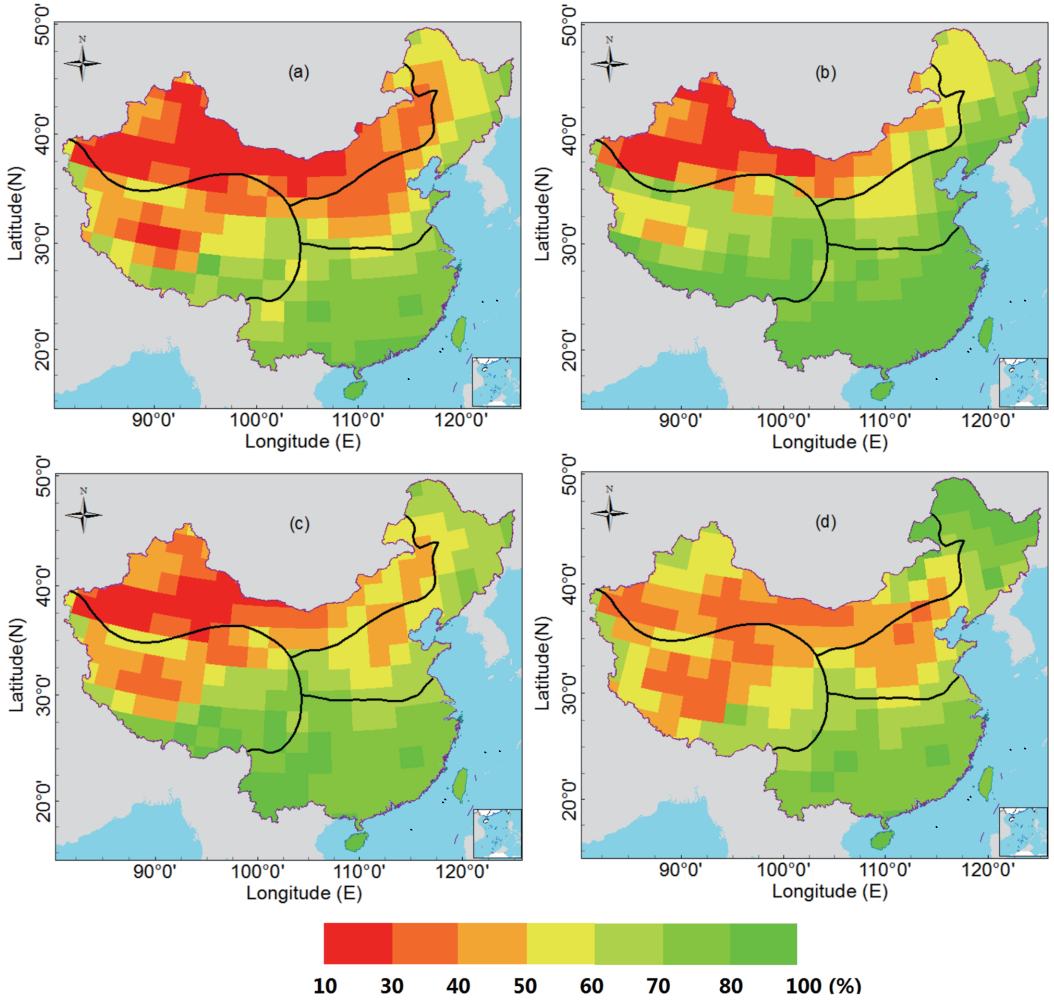

Fig. 9. As in Fig. 5 but for RH (%).

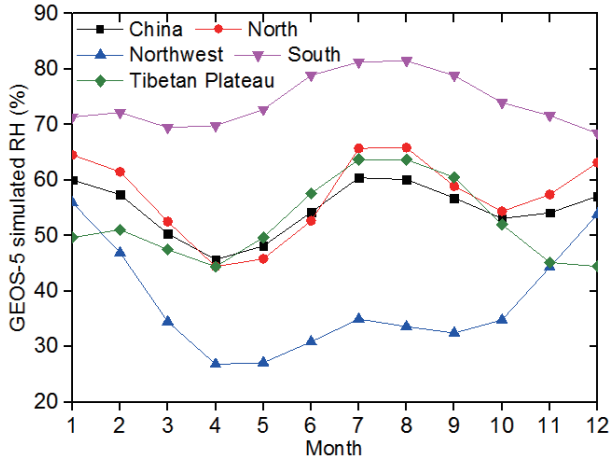

Fig. 10. As in Fig. 6 but for RH.

RH on $PM_{2.5}$ prediction is complex because the quality of modeled RH data varies in different regions, seasons, and dry–wet conditions, according to our validation. Most importantly, China's ground-based $PM_{2.5}$ network has been operational since 2013, while epidemiological studies usually require long-term $PM_{2.5}$ data. Therefore, estimating historical $PM_{2.5}$ levels would be very useful in China. For example, Ma et al. (2014) generated 10-year (2004–2013) mean $PM_{2.5}$ estimates in China and four sub-regions (including the Beijing–Tianjin metropolitan region, Yangtze River delta, Pearl River delta, and Sichuan Basin), and the interest in these data will likely be quite high within the global research community. Based on our analysis of the nine-year PBLH and RH using GEOS-5 data, the characteristics of the spatiotemporal distributions presented in this study can be used to improve the performance of $PM_{2.5}$ prediction models.

4. Conclusions

This analysis first validated the GEOS-5-simulated PBLH and RH using ground-based measurements. The PBLH values provided by GEOS-5 were similar over Wuhan but underestimated over Beijing compared to ground-based LIDAR data. Notably, obvious discrepancies were observed between the modeled values and in-situ observations in late summer and early autumn, as well as at the 0800 and 2000 LST sampling times. Due to the limited sample size, the quality of

the model-simulated PBLH remains unclear and is under investigation. We will perform further evaluations if additional ground-based LIDAR observations become available. When comparing the simulated RH values from the model and meteorological statistics, the coefficients of daily mean and monthly mean RH were 0.78 and 0.83, respectively. Overall, the RH data simulated from GEOS-5 can be used to determine the actual trends in different regions and periods. To the best of our knowledge, the accuracy of satellite-estimated $PM_{2.5}$ strongly depends on the quality of the PBLH and RH data. The comparison results presented in this analysis can be used to improve the process of obtaining satellite-derived $PM_{2.5}$.

Based on the satisfactory accuracy of the simulated results, the specific trends and distributions in the average PBLH and RH in different regions (North China, South China, Northwest China, and the TP) and seasons were discussed. The annual average PBLH values from 2004 to 2012 across China exhibited a narrow range (0.68–0.72 km). The highest PBLH values were observed in the TP region, which is affected by polar radiation and precipitation, followed by those in the Northwest and North China regions, with the lowest values in the South China region. Seasonally and monthly, large differences were observed among the four seasons, with higher values in summer and lower values in winter in all four regions. Additionally, high values were mainly concentrated from April to August, with the minimum value in December. Although the RH was obviously lower in summer, discrepancies and long-term variations were observed among the four regions, and no clear trend was identified at the regional or urban scales. Based on the regional divisions in this study, the climate in South China was the wettest due to abundant rainfall, whereas the RH in the Northwest China region, which includes desert areas, was less than 30%. Seasonally, the climate in the South China region was the most moderate. Northwest China was relatively wet in winter, with dry conditions in spring. Comparatively high values in other regions were mainly concentrated between July and September.

This analysis serves as a reference for studying the spatial and seasonal variations in the PBLH and RH and for further developing AOD–$PM_{2.5}$ models. However, the annual, seasonal and daily average PBLH and RH values do not meet the required accuracy of AOD–$PM_{2.5}$ models and cannot completely capture the associated dynamic changes. Therefore, in future work, PBLH and RH data from specific study periods will be extracted and applied to establish a more robust model for estimating the ground-level $PM_{2.5}$ mass concentration.

Acknowledgements. This work was supported by the National Key R&D Program of China (2016YFC0201507) and the National Natural Science Foundation of China (Grant Nos. 41471367, 91543128 and 41571417). We thank the National Meteorological Information Center and their staff for gathering and maintaining the data from the meteorological stations used in this investigation.

REFERENCES

Chen, Z. Y., W. Q. Liu, Y. J. Zhang, N. J. Zhao, and J. Ruan, 2009: Measurements of aerosol distribution by an elastic-backscatter lidar in summer 2008 in Beijing. *Chinese Optics Letters*, **7**, 753–755, https://doi.org/10.3788/COL20090709.0753.

Chi, R. L., D.-C. Wu, B. Liu, and J. Zhou, 2009: Dual-wavelength mie lidar observations of tropospheric aerosols. *Spectroscopy and Spectral Analysis*, **29**, 1468–1472, https://doi.org/10.3964/j.issn. 1000-0593(2009)06-1468-05.

Dandou, A., M. Tombrou, K. Schäfer, S. Emeis, A. P. Protonotariou, E. Bossioli, N. Soulakellis, and P. Suppan, 2009: A comparison between modelled and measured mixing-layer height over Munich. *Bound.-Layer Meteor.*, **131**, 425–440, https://doi.org/10.1007/s10546-009-9373-7.

Doukas, C., T. Pliakas, and I. Maglogiannis, 2010: Mobile healthcare information management utilizing cloud computing and Android OS. *Preprints, 2010 Annual International Conference of the IEEE Engineering in Medicine and Biology Society* (*EMBC*), Buenos Aires, IEEE, 1037–1040, https://doi.org/10.1109/IEMBS.2010.5628061.

Emeis, S., C. Munkel, S. Vogt, W. J. Müller, and K. Schäfer, 2004: Atmospheric boundary-layer structure from simultaneous SODAR, RASS, and ceilometer measurements. *Atmos. Environ.*, **38**, 273–286, https://doi.org/10.1016/j.atmosenv.2003.09.054.

Feng, J., H. Liao, and J. P. Li, 2016: The impact of monthly variation of the Pacific-North America (PNA) teleconnection pattern on wintertime surface-layer aerosol concentrations in the United States. *Atmos. Chem. Phys.*, **16**, 4927–4943, https://doi.org/10.5194/acp-16-4927-2016.

Gao, Y., M. Zhang, Z. Liu, L. Wang, P. Wang, X. Xia, M. Tao, and L. Zhu, 2015: Modeling the feedback between aerosol and meteorological variables in the atmospheric boundary layer during a severe fog-haze event over the North China Plain. *Atmos. Chem. Phys.*, **15**, 4279–4295, https://doi.org/10.5194/acp-15-4279-2015.

Guo, J.-P., and Coauthors, 2009: Correlation between PM concentrations and aerosol optical depth in eastern China. *Atmos. Environ.*, **43**, 5876–5886, https://doi.org/10.1016/j.atmosenv.2009.08.026.

Guo, J. P., and Coauthors, 2016: The climatology of planetary boundary layer height in China derived from radiosonde and reanalysis data. *Atmos. Chem. Phys.*, **16**, 13 309–13 319, https://doi.org/10.5194/acp-16-13309-2016.

Gupta, P., S. A. Christopher, J. Wang, R. Gehrig, Y. Lee, and N. Kumar, 2006: Satellite remote sensing of particulate matter and air quality assessment over global cities. *Atmos. Environ.*, **40**, 5880–5892, https://doi.org/10.1016/j.atmosenv.2006.03.016.

Hägeli, P., D. G. Steyn, and K. B. Strawbridge, 2000: Spatial and temporal variability of mixed-layer depth and entrainment zone thickness. *Bound.-Layer Meteor.*, **97**, 47–71, https://doi.org/10.1023/A:1002790424133.

Hayden, K. L., and Coauthors, 1997: The vertical chemical and meteorological structure of the boundary layer in the Lower Fraser Valley during Pacific '93. *Atmos. Environ.*, **31**, 2089–2105, https://doi.org/10.1016/S1352-2310(96)00300-7.

Hennemuth, B., and A. Lammert, 2006: Determination of the atmospheric boundary layer height from radiosonde and lidar backscatter. *Bound.-Layer Meteor.*, **120**, 181–200,

https://doi.org/10.1007/s10546-005-9035-3.

Hu, X.-M., J. W. Nielsen-Gammon, and F. Q. Zhang, 2010: Evaluation of three planetary boundary layer schemes in the WRF model. *J. Appl. Metorol. Clim.*, **49**, 1831–1844, https://doi.org/10.1175/ 2010JAMC2432.1.

Jones, R. H., S. Westra, and A. Sharma, 2010: Observed relationships between extreme sub-daily precipitation, surface temperature, and relative humidity. *Geophys. Res. Lett.*, **37**, L22805, https://doi.org/10.1029/2010GL045081.

Koelemeijer, R. B. A., C. D. Homan, and J. Matthijsen, 2006: Comparison of spatial and temporal variations of aerosol optical thickness and particulate matter over Europe. *Atmos. Environ.*, **40**, 5304–5315, https://doi.org/10.1016/j.atmosenv.2006.04.044.

Li, H., Y. Yang, X.-M. Hu, Z. W. Huang, G. Y. Wang, B. D. Zhang, and T. J. Zhang, 2017: Evaluation of retrieval methods of daytime convective boundary layer height based on lidar data. *J. Geophys. Res.*, **122**, 4578–4593, https://doi.org/10.1002/2016 JD025620.

Li, S., R. Kahn, M. Chin, M. J. Garay, and Y. Liu, 2015: Improving satellite-retrieved aerosol microphysical properties using GOCART data. *Atmospheric Measurement Techniques*, **8**, 1157–1171, https://doi.org/10.5194/amt-8-1157-2015.

Li, S. S., L. F. Chen, X. Z. Xiong, J. H. Tao, L. Su, D. Han, and Y. Liu, 2013: Retrieval of the haze optical thickness in North China Plain using MODIS data. *IEEE Transactions on Geoscience and Remote Sensing*, **51**, 2528–2540, https://doi.org/10.1109/TGRS.2012.2214038.

Li, S. S., C. Yu, L. F. Chen, J. H. Tao, H. Letu, W. Ge, Y. D. Si, and Y. Liu , 2016: Inter-comparison of model-simulated and satellite-retrieved componential aerosol optical depths in China. *Atmos. Environ.*, **141**, 320–332, doi: 10.1016/ j.atmosenv.2016.06.075.

Liu, J. J., J. P. Huang, B. Chen, T. Zhou, H. R. Yan, H. C. Jin, Z. W. Huang, and B. D. Zhang, 2015: Comparisons of PBL heights derived from CALIPSO and ECMWF reanalysis data over China. *Journal of Quantitative Spectroscopy and Radiative Transfer*, **153**, 102–112, https://doi.org/10.1016/j.jqsrt.2014.10.011.

Liu, X. G., and Coauthors, 2013: Formation and evolution mechanism of regional haze: A case study in the megacity Beijing, China. *Atmos. Chem. Phys.*, **13**, 4501–4514, https://doi.org/10.5194/ acp-13-4501-2013.

Liu, Y., R. J. Park, D. J. Jacob, Q. B. Li, V. Kilaru, and J. A. Sarnat, 2004: Mapping annual mean ground-level $PM_{2.5}$ concentrations using Multiangle Imaging Spectroradiometer aerosol optical thickness over the contiguous United States. *J. Geophys. Res.*, **109**, D22206, https://doi.org/10.1029/2004jd005025.

Lock, A. P., A. R. Brown, M. R. Bush, G. M. Martin, and R. N. B. Smith, 2000: A new boundary layer mixing scheme. Part I: Scheme description and single-column model tests. *Mon. Wea. Rev.*, **128**, 3187–3199, https://doi.org/10.1175/1520-0493(2000) 128<3187:ANBLMS>2.0.CO;2.

Luo, T., R. Yuan, and Z. Wang, 2014: Lidar-based remote sensing of atmospheric boundary layer height over land and ocean. *Atmospheric Measurement Techniques*, **7**, 173–182, https://doi.org/10.5194/amt-7-173-2014.

Ma, M. J., Z. X. Pu, S. G. Wang, and Q. Zhang, 2011: Characteristics and numerical simulations of extremely large atmospheric boundary-layer heights over an arid region in north-west China. *Bound.-Layer Meteor.*, **140**, 163–176, https://doi.org/10.1007/ s10546-011-9608-2.

Ma, Z. W., X. F. Hu, L. Huang, J. Bi, and Y. Liu, 2014: Estimating ground-level $PM_{2.5}$ in China using satellite remote sensing. *Environ. Sci. Technol.*, **48**, 7436–7444, https://doi.org/10.1021/ es5009399.

Ma, Z. W., and Coauthors, 2016: Satellite-based spatiotemporal trends in $PM_{2.5}$ concentrations: China, 2004-2013. *Environmental Health Perspectives*, **124**, 184–192, https://doi.org/10.1289/ ehp.1409481.

McGrath-Spangler, E. L., and A. Molod, 2014: Comparison of GEOS-5 AGCM planetary boundary layer depths computed with various definitions. *Atmos. Chem. Phys.*, **14**, 6717–6727, https://doi.org/10.5194/acp-14-6717-2014.

Medeiros, B., A. Hall, and B. Stevens, 2005: What controls the mean depth of the PBL? *J. Climate*, **18**, 3157–3172, https://doi.org/10.1175/JCLI3417.1.

Miao, Y. C., X.-M. Hu, S. H. Liu, T. T. Qian, M. Xue, Y. J. Zheng, and S. Wang, 2015: Seasonal variation of local atmospheric circulations and boundary layer structure in the Beijing-Tianjin-Hebei region and implications for air quality. *Journal of Advances in Modeling Earth Systems*, **7**, 1602–1626, https://doi.org/10.1002/2015MS000522.

Miao, Y. C., S. H. Liu, Y. J. Zheng, and S. Wang, 2016: Modeling the feedback between aerosol and boundary layer processes: A case study in Beijing, China. *Environmental Science and Pollution Research*, **23**, 3342–3357, https://doi.org/10.1007/s11356-015-5562-8.

Moradi, I., P. Arkin, R. Ferraro, P. Eriksson, and E. Fetzer, 2016: Diurnal variation of tropospheric relative humidity in tropical regions. *Atmos. Chem. Phys.*, **16**, 6913–6929, https://doi.org/10.5194/ acp-16-6913-2016.

Quan, J. N., and Coauthors, 2013: Evolution of planetary boundary layer under different weather conditions, and its impact on aerosol concentrations. *Particuology*, **11**, 34–40, https://doi.org/10.1016/j.partic.2012.04.005.

Seibert, P., F. Beyrich, S.-E. Gryning, S. Joffre, A. Rasmussen, and P. Tercier, 2000: Review and intercomparison of operational methods for the determination of the mixing height. *Atmos. Environ.*, **34**, 1001–1027, doi: 10.1016/S1352-2310(99) 00349-0.

Seidel, D. J., Y. H. Zhang, A. Beljaars, J.-C. Golaz, A. R. Jacobson, and B. Medeiros, 2012: Climatology of the planetary boundary layer over the continental United States and Europe. *J. Geophys. Res.*, **117**, D17106, https://doi.org/10.1029/2012jd018143.

Stott, P., 2016: How climate change affects extreme weather events. *Science*, **352**, 1517–1518, doi: 10.1126/science.aaf 7271.

Sun, Y. L., and Coauthors, 2016: Rapid formation and evolution of an extreme haze episode in Northern China during winter 2015. *Scientific Reports*, **6**, 27151, https://doi.org/10.1038/srep27151.

Tao, J. H., M. G. Zhang, L. F. Chen, Z. F. Wang, L. Su, C. Ge, X. Han, and M. M. Zou, 2013: A method to estimate concentrations of surface-level particulate matter using satellite-based aerosol optical thickness. *Science China Earth Sciences*, **56**, 1422–1433, https://doi.org/10.1007/s11430-012-4503-3.

Veerabuthiran, S., A. K. Razdan, M. K. Jindal, D. K. Dubey, and R. C. Sharma, 2011: Mie lidar observations of lower tropospheric aerosols and clouds. *Spectrochimica Acta Part A: Molecular and Biomolecular Spectroscopy*, **84**, 32–36, https://doi.org/10.1016/j.saa.2011.08.021.

Vergados, P., A. J. Mannucci, C. O. Ao, J. H. Jiang, and H. Su, 2015: On the comparisons of tropical relative humidity in the lower and middle troposphere among COSMIC radio occultations and MERRA and ECMWF data sets. *Atmospheric Measurement Techniques*, **8**, 1789–1797, https://doi.org/10.5194/amt-8-1789-2015.

Wang, J., and S. A. Christopher, 2003: Intercomparison between satellite-derived aerosol optical thickness and $PM_{2.5}$ mass: Implications for air quality studies. *Geophys. Res. Lett.*, **30**, 2095, https://doi.org/10.1029/2003gl018174.

Wang, Z. F., L. F. Chen, J. H. Tao, Y. Zhang, and L. Su, 2010: Satellite-based estimation of regional particulate matter (PM) in Beijing using vertical-and-RH correcting method. *Remote Sensing of Environment*, **114**, 50–63, https://doi.org/10.1016/j.rse.2009.08.009.

Xu, C. C., J. Zhao, J. X. Li, S. T. Gao, R. P. Zhou, H. Z. Liu, and Y. P. Chen, 2015: Climate change in Urumqi City during 1960-2013. *Quaternary International*, **358**, 93–100, https://doi.org/10.1016/j.quaint.2014.11.062.

Zhang, G. H., Z. C. Li, Y. Song, Y. L. Wu, and X. L. Wang, 2011: Spatial patterns of change trend in rainfall of China and the role of East Asia summer monsoon. *Arid Land Geography*, **34**, 34–42. (in Chinese)

Zhang, W. C., J. P. Guo, Y. C. Miao, H. Liu, Y. Zhang, Z. Q. Li, and P. M. Zhai, 2016: Planetary boundary layer height from CALIOP compared to radiosonde over China. *Atmos. Chem. Phys.*, **16**, 9951–9963, https://doi.org/10.5194/acp-16-9951-2016.

Zhang, Y., X.-Y. Wen, and C. J. Jang, 2010: Simulating chemistry-aerosol-cloud-radiation-climate feedbacks over the continental U.S. using the online-coupled Weather Research Forecasting Model with chemistry (WRF/Chem). *Atmos. Environ.*, **44**, 3568–3582, https://doi.org/10.1016/j.atmosenv.2010.05.056.

Zhang, Y. H., S. D. Zhang, C. M. Huang, K. M. Huang, Y. Gong, and Q. Gan, 2014: Diurnal variations of the planetary boundary layer height estimated from intensive radiosonde observations over Yichang, China. *Science China Technological Sciences*, **57**, 2172–2176, https://doi.org/10.1007/s11431-014-5639-5.

Zhang, Z. Z., X. H. Cai, Y. Song, L. Kang, X. Huang, and Q. Y. Li, 2013: Temporal and spatial variation of atmospheric boundary layer height over Hainan Island and its adjacent sea areas. *Acta Scientiarum Naturalium Universitatis Pekinensis*, **49**, 783–790. (in Chinese)

Zhou, L., X. D. Xu, G. A. Ding, M. Y. Zhou, and X. H. Cheng, 2005: Diurnal variations of air pollution and atmospheric boundary layer structure in Beijing during winter 2000/2001. *Adv. Atmos. Sci.*, **22**, 126–132, https://doi.org/10.1007/BF02930876.

Zhu, Y. L., H. J. Wang, W. Zhou, and J. H. Ma, 2011: Recent changes in the summer precipitation pattern in east China and the background circulation. *Climate Dyn.*, **36**, 1463–1473, https://doi.org/10.1007/s00382-010-0852-9.

Fernald, F., Herman, M., Reagan, J., 1972: Determination of aerosol height distributions by Lidar. *Journal of Applied Meteorology*, **11**, 482–489, https://doi.org/10.1175/1520-0450(1972)011 <0482:DOAHDB>2.0.CO;2.

Louis, J., Tiedtke, M., and Geleyn, J., 1982: A short history of the PBL parameterization at ECMWF, *Workshop on Planetary Boundary Layer Parameterization*, ECMWF, Reading, England, 5–27 November 1981, 59–79.

Menut, L., C. Flamant, J. Pelon, and P. H. Flamant, 1999: Urban boundary-layer height determination from lidar measurements over the Paris area. *Appl. Optics*, **38**, 945-954.

Song, Y. F., Y. J. Liu, and Y. H. Ding, 2012: A study of surface humidity changes in china during the recent 50 years. *Acta Meteorologica Sinica*, **26**, 541-553.